Journal of Dynamics, Monitoring and Diagnostics, 2025, 4, 226-238
https://doi.org/10.37965/jdmd.2025.813

ISTP
RESEARCH ARTICLE

Enhancing SDP-CNN for Gear Fault Detection Under Variable Working Conditions via Multi-Order Tracking Filtering

Mario Spirto, Armando Nicolella, Francesco Melluso, Pierangelo Malfi, Chiara Cosenza, Sergio Savino, and Vincenzo Niola

Department of Industrial Engineering, University of Naples Federico II, Naples, Italy

(Received 09 May 2025; Revised 26 May 2025; Accepted 01 July 2025; Published online 02 July 2025)

Abstract: In the field of gear fault detection, the symmetrized dot pattern (SDP) technique, combined with a convolutional neural network (CNN), is widely used to classify various types of defects. The SDP-CNN combination is used to transform vibration signals and simplify the defect classification process under stationary operating conditions. This work aims to enhance the SDP-CNN combination for detecting incipient defects in gear under variable working conditions. The vibration signals are filtered by Vold-Kalman Filter Multi-Order Tracking to highlight fault characteristics under variable working conditions. Subsequently, the signals are SDP-transformed and are then classified by optimized CNN. The new pipeline has been validated on an experimental dataset and compared with the classical one by developing both two- and multi-class CNNs. The results showed the applicability of the new pipeline in terms of percentage accuracy and ROC curve compared to the classical approach. Finally, the proposed pipeline was compared with other ML literature techniques using the same dataset.

Keywords: convolutional neural network; fault detection; order tracking; symmetrized dot pattern; vibrational signal processing

I. INTRODUCTION

Fault detection (FD) is a crucial part of predictive maintenance. It is the process of monitoring and identifying malfunctions, anomalies, and faults of the mechanical systems. The main objective is to detect any variation from the expected behavior to prevent greater damage and reduce downtime [1,2].

Zhi *et al.* [3] had developed a new algorithm to detect gearbox faults through meshing frequency modulation (MFM) analysis and a definition of a new index to generate a MFMgram. El Yousfi *et al.* [4] had developed a physical model of an electric motor and a gearbox to detect gear teeth break and crack under stationary and non-stationary working conditions. Recently, new methods for FD of planetary gearboxes under non-stationary conditions have been developed through order tracking [5], residual signal energies [6], improved variational mode decomposition (VMD) [7], and pattern recognition [8,9]. Yuan *et al.* [10] had improved the synchrosqueezing wavelet transform (WT) to detect gearbox faults in high noise and transient condition. Tao *et al.* [11] had projected a robust statistical descriptor WT and Gaussian density modeling to detect bearing faults. Li *et al.* [12] proposed the heterogeneous signal embedding module, a plug-and-play component that unifies fault diagnosis across diverse signals with varying sampling rates and lengths. In addition, they introduced an interpretable neural network using learnable Morlet wavelet operators, gated matrices, and skip connections to enhance fault signature extraction, boosting transparency, and performance in mechanical fault diagnosis [13].

Nowadays, the use of ML techniques has become widespread in FD of mechanical systems, thanks to their ability to identify anomalies, detect early faults, and optimize predictive maintenance strategies [14]. Innovative deep learning architecture to filter and extract fault features from accelerometric signals to detect bearing faults was presented in [15]. The lack of a failure condition dataset to train the ML classification model can be fixed using physical models [16] or generative adversarial networks [17] and finally testing the model to validate it. Ravikumar *et al.* [18] developed an ML model composed of a convolutional neural network (CNN) and a long short-term memory to detect faults in gearbox: the first was used for feature extraction, while the second was used for feature selection. A feedforward neural network (FNN) based on accelerometer signals has been developed for the FD of aircraft hybrid electric propulsion systems [19].

The symmetrized dot pattern (SDP) technique has emerged as a tool for signal analysis, providing a signal transformation to facilitate system anomaly detection with significant applications in diagnostics and predictive maintenance [20]. An advantage of the SDP technique over raw signal analysis is its ability to convert complex, non-linear, and non-stationary signals into easily visual representations. This facilitates the identification and classification of operating conditions or faults in mechanical systems [21]. A study has shown that FD based on the SDP transformation of vibrational signals significantly increases process accuracy compared to other transformation techniques [22]. Thanks to SDP signal transformation, it is possible to automate the FD process by means of existing or purpose-built CNN [23–25]. The transformation of vibrational [26], acoustic [27], or different sensor signals [28] using SDP makes it possible to achieve high classification accuracy thanks to CNNs.

Song *et al.* [29] proposed a transfer learning method to extract and classify bearing defects using SDP. Zhang *et al.* [30] demonstrated the SDP potential to predict wear-cutting

Corresponding author: Mario Spirto (e-mail: mario.spirto@unina.it).

tools using a multi-covariance Gaussian process regression. Xu *et al.* [31] presented a matching technique of snowflake diagrams using templates derived from signals' SDP transformation for fan FD, and they implemented the technique in real time [32]. The Empirical Mode Decomposition and VMD are widely used to improve the accuracy of CNNs [33–35]. Liu *et al.* [36] developed a new CNN architecture for FD under stationary and time-varying gearbox working conditions using different accelerometers to obtain the SDP diagram. The technique was experimentally validated on a test bench demonstrating high classification accuracy and a low false positive rate.

The SDP allows recurring patterns or anomalies in vibration signals to be visualized graphically, facilitating the identification of mechanical faults through symmetrical representations. Compared to raw signal analysis, SDP provides greater clarity and ease of identification of distinguishing features, improving the FD process using CNNs. FD based on SDP and CNN is almost always performed under stationary operating conditions due to the high variability of the snowflake diagram. In real practice, many plants operate under variable working conditions, hence the need to implement FD techniques under such conditions.

This work aims to provide an effective approach to enhance the SDP-CNN combination to detect incipient gear faults under speed and load variable working conditions. The proposed method involves extracting the Gear-Meshing Order (GMO) of the Faulty Gear (FG), and the Coupled Gear (CG) on the same shaft, to highlight the system fault characteristics. This operation was carried out by implementing a Vold-Kalman Filter Multi-Order Tracking (VKF_MOT): this filter allows to extract fault signatures from the signal under variable working conditions. The filtered signal was then transformed into SDP coordinates. Finally, a designed and optimized CNN was introduced to predict the gear condition. The proposed methodology was tested on an experimental dataset that includes several operating conditions, both stationary and time-varying, and various incipient defects. The method validation was carried out by developing several two-class CNNs comparing the health state and the incipient defect. A multi-class CNN was also developed to provide a technique capable of identifying the defect type. The proposed method VKF_MOT-SDP-CNN was compared with the traditional SDP-CNN pipeline to demonstrate the low accuracy of the classic approach to FD under variable working conditions. The comparison showed that the proposed method is more accurate and has a lower false positive rate than the classic approach. Finally, the VKF_MOT-SDP-CNN was compared with other ML classification algorithms applied to the same dataset.

The main contributions of this work can be summarized as follows:

1. A new pipeline VKF_MOT-SDP-CNN was developed for FD using SDP in variable working conditions for different kinds of incipient defects to enhance the SDP-CNN FD process.
2. The new pipeline was tested on the experimental dataset by using a two-class CNN and compared to the classic SDP-CNN approach.
3. The new pipeline was tested by using a multi-class CNN and compared to the classic SDP-CNN approach.
4. The VKF_MOT-SDP-CNN was compared with other ML algorithms.

The rest of this article is structured as follows: the dataset description is presented in Section II; the methodology is described in Section III; the results are discussed in Section IV; and finally, Section V summarizes the conclusions of this work.

II. EXPERIMENTAL DATASET

The experimental data were provided from the "MCC5-THU gearbox fault diagnosis dataset" which includes vibration, speed, and torque signals under variable working conditions, different gearbox faults, and severity degree [37]. The dataset was collected from a two-stage parallel gearbox where the gear on the intermediate shaft is the FG. Each signal was sampled at 12.8 kHz for 60 seconds. Figure 1 shows the gearbox test rig and the parallel gearbox internal structure.

In this work, the signals reported in Table I were used. These signals are featured by a light severity degree of gear faults, a double trapezoidal load-time curve, and a ramp speed-time curve. Signals with light severity degree defects were selected to demonstrate that the proposed technique can detect an incipient fault.

Figure 2 shows the gearbox input speeds and torques for signals number 1 and 2 of Table I. In Fig. 2, it is possible to see the speed and the torque transients highlighted by the gray zone. The speed transients are a ramp that goes from 0

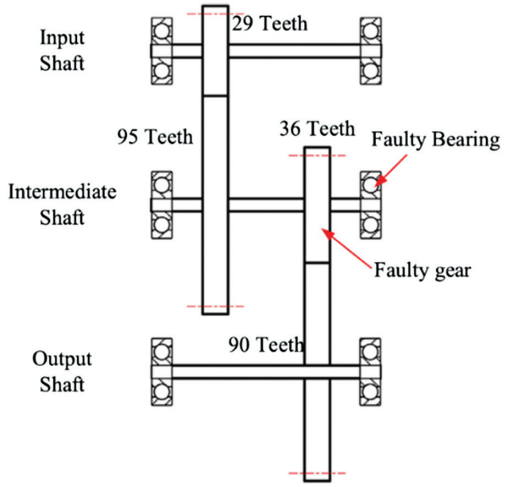

Fig. 1. Schematic gearbox overview.

Table I. Signal list

Signal number	Gear condition	Defect description
1	Healthy	/
2	Healthy	/
3	Light Wear	1/3 of the teeth surface area
4	Light Wear	1/3 of the teeth surface area
5	Light Gear Pitting	Fault diameter 0.5 mm
6	Light Gear Pitting	Fault diameter 0.5 mm
7	Light Teeth Break	¼ of the teeth width
8	Light Teeth Break	¼ of the teeth width

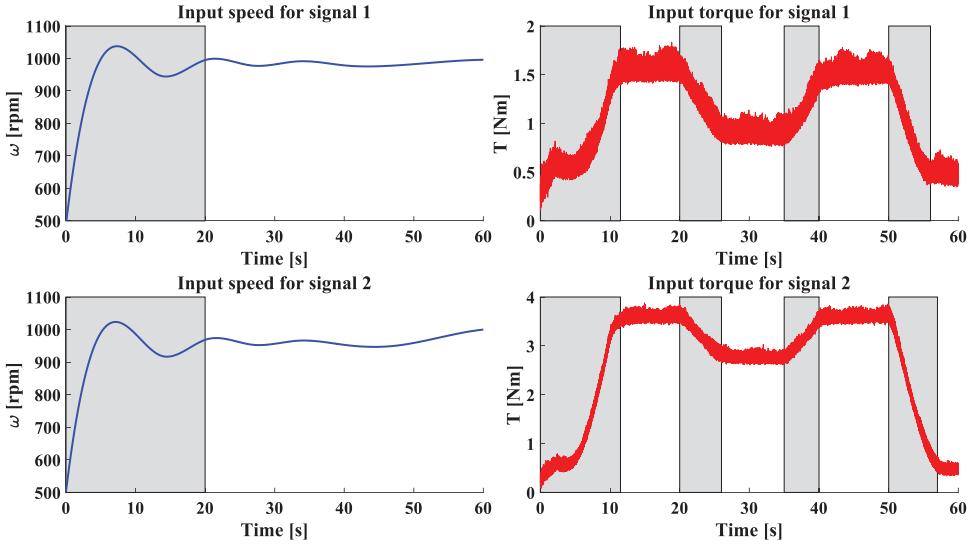

Fig. 2. Gearbox input speeds and torques for healthy signals.

to 20 seconds, while the torque time-varying curves are a double trapezoidal curve.

III. FD STRATEGY UNDER VARIABLE WORKING CONDITIONS: DEVELOPMENT STEPS

The FD-developed strategy under variable working conditions can be viewed as the task of extracting modulating diagnostic components from a non-stationary, and noisy vibration signal, when the fundamental frequency changes over time and the fault is localized. Traditional methods based on the SDP-CNN approach have demonstrated effectiveness under stationary conditions, but their sensitivity to dynamic changes limits their applicability in real-world scenarios. To overcome these limitations, it is proposed to integrate the VKF_MOT as a pre-processing step for vibration signals. It is renowned for its capability to extract specific harmonic components from complex and non-stationary signals, thereby enhancing the robustness of fault diagnosis under variable operating conditions. The integration of VKF_MOT allows for the isolation of frequency components associated with faults, reducing the influence of noise and non-stationary variations. This process improves the quality of the generated SDP images, providing more representative inputs for the CNN and increasing the accuracy of fault classification. Furthermore, the VKF_MOT-SDP-CNN pipeline eliminates the need for complex time-frequency transformations, preserving the integrity of temporal information and reducing the risk of phase distortions. This characteristic is particularly advantageous for analyzing vibration signals under variable working conditions, where non-stationarity is an intrinsic feature. The proposed approach combines the strengths of VKF in handling non-stationary signals with CNN capability to perform accurate classifications based on SDP images, offering an effective solution for fault diagnosis in complex industrial scenarios.

The developed algorithm is shown in Fig. 3. As shown in Fig. 3:

1. The first step of the algorithm is to extract the GMOs of FG and CG using VKF_MOT from the vibrational signals. Using this filter enables the extraction of the FG and CG fault signatures from the signal under variable working conditions.
2. The second step of the algorithm is to transform the filtered signal using the SDP.
3. The third step of the algorithm is to develop the CNN for gear FD.

A. NON-STATIONARY VIBRATIONAL SIGNALS

In scenarios involving variable speed and load, the vibrational signal $y(t)$ acquired from a rotating gearbox system is typically non-stationary, meaning its statistical properties change over time. A formal model can be expressed as:

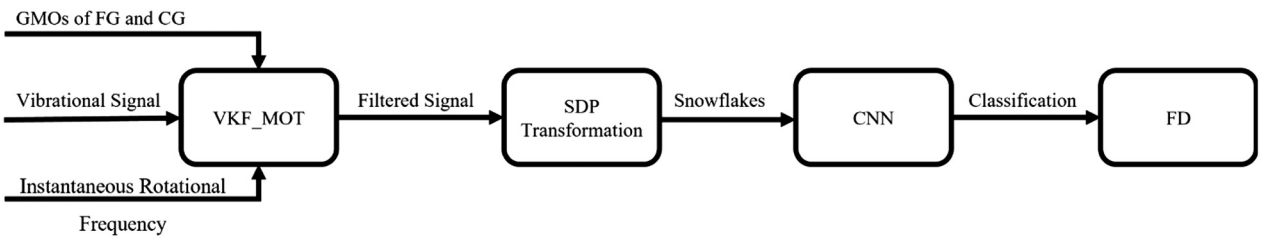

Fig. 3. Algorithm steps for gear health status prediction.

$$y(t) = \sum_{k=1}^{K} A_k(t) \cos\left(2\pi \int_0^t f_k(\tau) d\tau + \phi_k(t)\right) + \eta(t) \quad (1)$$

where:

- $A_k(t)$ is the time-varying amplitude of the k-th harmonic component.
- $f_k(t) = k \cdot f(t)$ is the instantaneous frequency, the k-th multiple of the non-stationary rotational frequency $f(t)$.
- $\phi_k(t)$ is the non-stationary phase term.
- K is the number of GMOs harmonics.
- $\eta(t)$ is Gaussian additive noise and other not target components.

Under stationary conditions can be written:

$$f(t) = f_0 \quad (2)$$

where f_0 is the constant rotational instantaneous frequency, and the signal $y(t)$ is periodic. If equation (2) is not valid, $y(t)$ is non-stationary and $f(t)$ changes over time.

This non-stationarity undermines the effectiveness of the SDP, which assumes constant periodicity for a stable representation in the polar domain. Additionally, it complicates the identification of diagnostic components related to faults. To tackle this challenge, a VKF_MOT is proposed to pre-filter the non-stationary signal $y(t)$. The filter isolates components:

$$A_k(t) \cos\left(2\pi \int_0^t f_k(\tau) d\tau + \phi_k(t)\right) \quad (3)$$

that corresponds to desired GMOs, attenuating $\eta(t)$, and the resulting signal $y_f(t)$ contains only the desired components to make SDP snowflake diagram stable.

B. VKF_MOT IMPLEMENTATION

The VKF_MOT is a passband adaptive filter to extract non-stationary periodic components from vibration or acoustic signals of the rotating machine if its instantaneous rotational frequency is known [38,39]. The problem is defined by solving two equations, the structural and the data equation, using the method of least squares. The equations smooth the unknown complex envelopes. They relate the tracked orders to the measured signal.

The discrete signal $y(n)$ obtained from a rotating machine contains K components $x_k(n)$, each of which is associated with an order related to the rotation of the machine and represents a signal to be tracked. However, these components are contaminated by random noise and other irrelevant periodic components denoted by $\epsilon_k(n)$. Each order $x_k(n)$ is also modeled as a solution to a second-order differential equation, which allows an accurate description of the dynamics within the system. Then, it is possible to write the k-order as:

$$x_k(n) - 2\cos(\omega_k(n)\Delta T) x_k(n-1) + x_k(n-2) = \epsilon_k(n) \quad (4)$$

Where $\omega_k(n) = k \cdot \omega(n)$ and $\omega(n)$ is the angular frequency. The equation (4) can be rewritten in status form defining:

$$\underline{x}_k(n) = \begin{bmatrix} x_k(n-1) \\ x_k(n) \end{bmatrix} \quad (5)$$

$$\underline{x}_k(n+1) = \begin{bmatrix} x_k(n) \\ x_k(n+1) \end{bmatrix} \quad (6)$$

The equations (5) and (6) allow the equation (4) to be rewritten as a linear relationship between consecutive states. The equation (4) can be written for the $n+1$ iteration as:

$$x_k(n+1) - 2\cos(\omega_k(n)\Delta T) x_k(n) + x_k(n-1) = \epsilon_k(n) \quad (7)$$

$$x_k(n+1) = 2\cos(\omega_k(n)\Delta T) x_k(n) - x_k(n-1) + \epsilon_k(n) \quad (8)$$

and in matrix form:

$$\begin{bmatrix} x_k(n) \\ x_k(n+1) \end{bmatrix} = \begin{bmatrix} 0 & 1 \\ -1 & 2\cos(\omega_k(n)\Delta T) \end{bmatrix} \begin{bmatrix} x_k(n-1) \\ x_k(n) \end{bmatrix} + \begin{bmatrix} 0 \\ \epsilon_k(n) \end{bmatrix} \quad (9)$$

and substituting with the equations (5) and (6) in the equation (9):

$$\underline{x}_k(n+1) = \boldsymbol{M}_k(n) \underline{x}_k(n) + \underline{\epsilon}_k(n) \quad (10)$$

where:

$$\boldsymbol{M}_k(n) = \begin{bmatrix} 0 & 1 \\ -1 & 2\cos(\omega_k(n)\Delta T) \end{bmatrix} \quad (11)$$

$$\underline{\epsilon}_k(n) = \begin{bmatrix} 0 \\ \epsilon_k(n) \end{bmatrix} \quad (12)$$

The equation (10) is a recursive matrix relation. To track K multiple order components simultaneously, it is necessary to concatenate all state vectors into a global state vector:

$$\boldsymbol{X}(n) = \begin{bmatrix} \underline{x}_1(n) \\ \underline{x}_2(n) \\ \vdots \\ \underline{x}_K(n) \end{bmatrix} \quad (13)$$

$$\boldsymbol{X}(n+1) = \begin{bmatrix} \underline{x}_1(n+1) \\ \underline{x}_2(n+1) \\ \vdots \\ \underline{x}_K(n+1) \end{bmatrix} \quad (14)$$

and let the diagonal matrix:

$$\boldsymbol{F}(n+1,n) = \begin{bmatrix} \boldsymbol{M}_1(n) & 0 & 0 & 0 & \cdots & 0 & 0 \\ 0 & \boldsymbol{M}_2(n) & 0 & 0 & \cdots & 0 & 0 \\ 0 & 0 & \boldsymbol{M}_3(n) & 0 & \cdots & 0 & 0 \\ \vdots & \vdots & \vdots & \vdots & \ddots & \vdots & \vdots \\ 0 & 0 & 0 & 0 & \cdots & 0 & \boldsymbol{M}_K(n) \end{bmatrix} \quad (15)$$

and defined:

$$\boldsymbol{E}(n) = \begin{bmatrix} \underline{\epsilon}_1(n) \\ \underline{\epsilon}_2(n) \\ \vdots \\ \underline{\epsilon}_K(n) \end{bmatrix} \quad (16)$$

the equation (4) for K multiple order components simultaneously tracked became:

$$\boldsymbol{X}(n+1) = \boldsymbol{F}(n+1,n)\boldsymbol{X}(n) + \boldsymbol{E}(n) \tag{17}$$

The equation (17) is the structural equation of VKF_MOT.

The measured signal $y(n)$ to track multiple order components simultaneously can be written as:

$$y(n) = x_K(n) + \eta(n) = \sum_{k=1}^{K} x_k(n) + \eta(n) \tag{18}$$

where $\eta(n)$ is a random Gaussian noise and other not targets periodic components. Expressing the equation (18) as a state vector:

$$y(n) = \boldsymbol{I}(n)\boldsymbol{X}(n) + \eta(n) \tag{19}$$

that is the data equation of VKF_MOT where:

$$\boldsymbol{I}(n) = [\underline{I}_1(n)\ \underline{I}_2(n)\ \cdots\ \underline{I}_K(n)] \tag{20}$$

$$\underline{I}_k(n) = [0 \quad 1] \tag{21}$$

If the instantaneous frequency $\omega_k(n)$ is known, the k-order non-stationary component $x_k(n)$ can be evaluated as:

$$\underline{x}_k(n) = \left[\cos\left(\sum_{m=0}^{n}\omega_k(m)\Delta T\right)\sin\left(\sum_{m=0}^{n}\omega_k(m)\Delta T\right)\right]\begin{bmatrix}a_k(n)\\ b_k(n)\end{bmatrix} \tag{22}$$

where the amplitude of $\underline{x}_k(n)$ is obtained by $\sqrt{a_k(n)^2 + b_k(n)^2}$.

Since equations (17) and (19) are written identically to the process and measurement equations of the Kalman filter, they can be solved as illustrated in [40].

The obtained $x_K(n)$ is used as the input signal for SDP transformation.

C. SDP TRANSFORMATION

The SDP is a technique that transforms a time signal into a normalized point plane by creating a symmetrical scatter plot of amplitudes on a polar diagram called a "snowflake" [20].

This method allows a visual representation of signal amplitude and frequency variations, simplifying fault diagnosis in rotating systems such as gears. SDP improves the FD process by providing greater clarity and easier identification of features compared to raw signal analysis [21,22]. The difference between signals can be seen in the shape of the petals that make up the snowflake diagram. The diagram uses h planes of symmetry by rotating the petals by an angle:

$$\vartheta = \frac{360}{h} \tag{23}$$

A necessary condition to plot the snowflake is that the petals do not overlap.

It is possible to transform $x_K(n)$ in polar coordinates using the SDP transform by the formula:

$$r(i) = \frac{x_K(i) - \max(x_K(n))}{\max(x_K(n)) - \min(x_K(n))} \tag{24}$$

$$\theta(i) = \vartheta + \frac{x_K(i+l) - \min(x_K(n))}{\max(x_K(n)) - \min(x_K(n))}\xi \tag{25}$$

$$\Phi(i) = \vartheta - \frac{x_K(i+l) - \min(x_K(n))}{\max(x_K(n)) - \min(x_K(n))}\xi \tag{26}$$

where:

- $\min(x_K(n))$ and $\max(x_K(n))$ are the minimum and the maximum value of $x_K(n)$ respectively.
- $r(i)$ is the radius of the i-th point.
- $\theta(i)$ is the clockwise deflection angle of the i-th point along the symmetry plane.
- $\Phi(i)$ is the anticlockwise deflection angle of the i-th point along the symmetry plane.
- l is the delay coefficient.
- ϑ is the rotation angle of the symmetry plane.
- ξ is the gain of the deflection angle.

Figure 4 shows the influence of ξ and l in the snowflake diagram: as ξ increases, the petal curvature will be greater, while as l increases, the petal width will be greater.

After setting the optimal ξ and l parameters [41], it is possible to transform $x_K(n)$ into the snowflake diagram and thus obtain the CNN input images.

D. CNN DEVELOPMENT AND OPTIMIZATION

The images generated by the SDP are first converted to binary images as shown in Fig. 5. and then processed by the proposed CNN algorithm.

A CNN is a type of artificial neural network (ANN) specifically designed to process image datasets using a grid-based structure, making it suitable for image classification tasks [42]. The proposed supervised CNN learns a mapping between the input image, derived from the SDP algorithm, and the corresponding output, allowing the classification of the fault category associated with the image.

The input layer processes single-channel binary images. The network uses an optimized depth convolutional architecture where both the number of layers and the hyperparameters are Bayesian optimized [43].

Each convolutional block follows a structured sequence involving a convolutional layer, batch normalization (BN), a rectified linear unit (ReLU) as the activation function, and a max-pooling layer. This process can be expressed mathematically as:

$$X^{(l+1)} = \max(ReLU(BN(X^l * W^l))) \tag{27}$$

where W^l is the convolution kernel of size $k \times k$, l is the generic convolutional block, X is the input image, and * is the convolution operator.

The BN function normalizes the feature maps $(X^l * W^l)$ to stabilize training, while ReLU introduces non-linearity into the network by allowing positive values to pass unaltered and setting negative values to zero. The number of convolutional filters W^l is optimized by Bayesian optimization to improve the feature extraction. Finally, in the convolutional block is applied the max-pooling which is the maximum value within a defined pooling window to reduce the spatial dimensionality of the feature map.

After the final convolutional block, the flattened final pooling layer is given to the fully FNN, where the ReLU is used as the activation function, and a SoftMax function converts the raw output scores into a probability distribution over the classes.

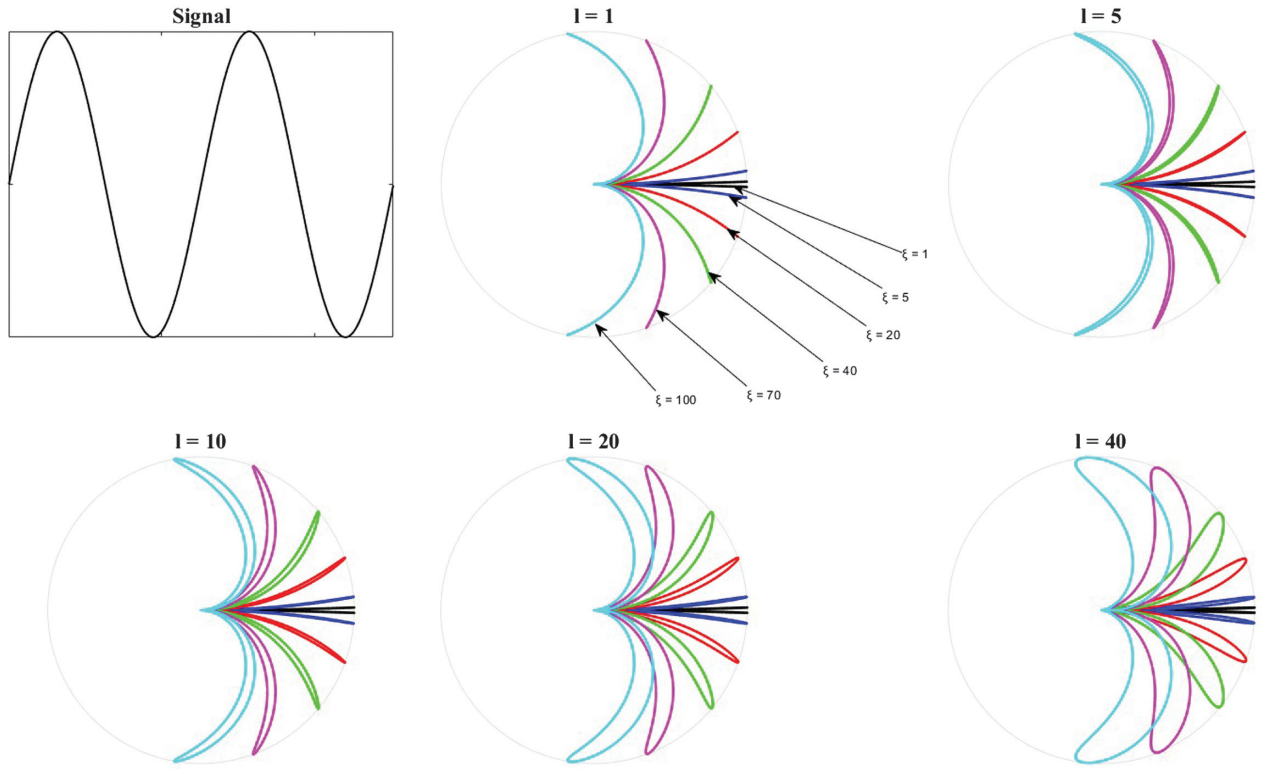

Fig. 4. Snowflake dependency from ξ and *l*.

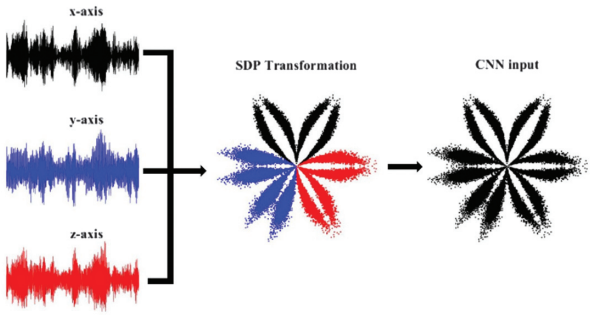

Fig. 5. CNN input image development.

The loss function used in the proposed CNN is the cross-entropy loss, which is widely used in classification tasks to measure the difference between the predicted probability distribution and the true class labels. The proposed CNN algorithm employs Stochastic gradient descent with momentum (SGDM) as the optimization method. The Bayesian optimization process aims to minimize the expected loss over the space of hyperparameters. It is formulated as:

$$\mathcal{O}(\theta) = E\left[L(\theta)\right] \tag{28}$$

where θ represents the vector of chosen hyperparameters, and $E[L(\theta)]$ shows the expected value of the loss function under the current hyperparameter configuration.

Bayesian optimization efficiently searches the hyperparameter space using probabilistic models to find the best combination without requiring an exhaustive grid search.

A generic proposed CNN architecture is shown in Fig. 6.

IV. RESULTS AND DISCUSSION

All three axes were considered in this study to fully capture the vibrational behavior of the gearbox. Figure 7 shows the normalized raw and filtered vibration signals for signal 1 of Table I.

GMO represents the fundamental order in which meshing occurs between the teeth of two gears. Multiples of this frequency can be influenced by defects in the teeth such as wear or local breaks. The analysis of these harmonics enables the identification and characterization of such defects.

In particular, the analysis of the first harmonics of GMO is widely recognized in the literature as effective for FD in mechanical transmission systems, and the defects in the FG are visible in the CG GMOs since the FG meshes directly with the CG [44,45].

The signals were acquired at a frequency of 12800 Hz. According to the Shannon-Nyquist theorem, the visible frequency limit is 6400 Hz. The rotation speed of the FG corresponds to the maximum input speed of the gearbox, approximately 1000 rpm (which equals about 16.67 Hz), considering the 29/95 transmission ratio (Fig. 1).

Therefore, the maximum visible order considering the rotational speed of the shaft on which the FG is coupled is given by the following equation:

$$\mathcal{O}_{\max} = \frac{f_s}{2f_r}\frac{1}{\varepsilon} = \frac{12800}{2 \cdot 16.67}\frac{95}{29} \approx 1257 \tag{29}$$

where f_s is the sampling frequency, f_r is the input rotation frequency, and ε is the transmission ratio. Since beyond order 300 there is a significant reduction in amplitudes in the order spectrum of Fig. 8, only orders below this value were selected. As reported in Fig. 1, since the FG has 36 teeth and the CG has 90 teeth, the selected multiple order values are:

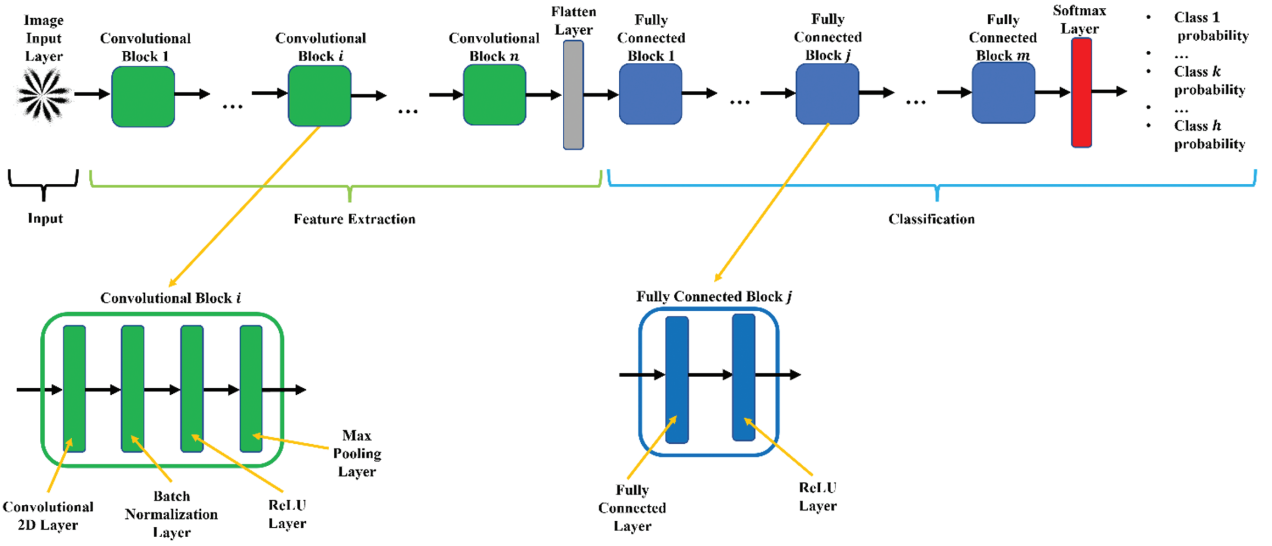

Fig. 6. Generic proposed CNN architecture.

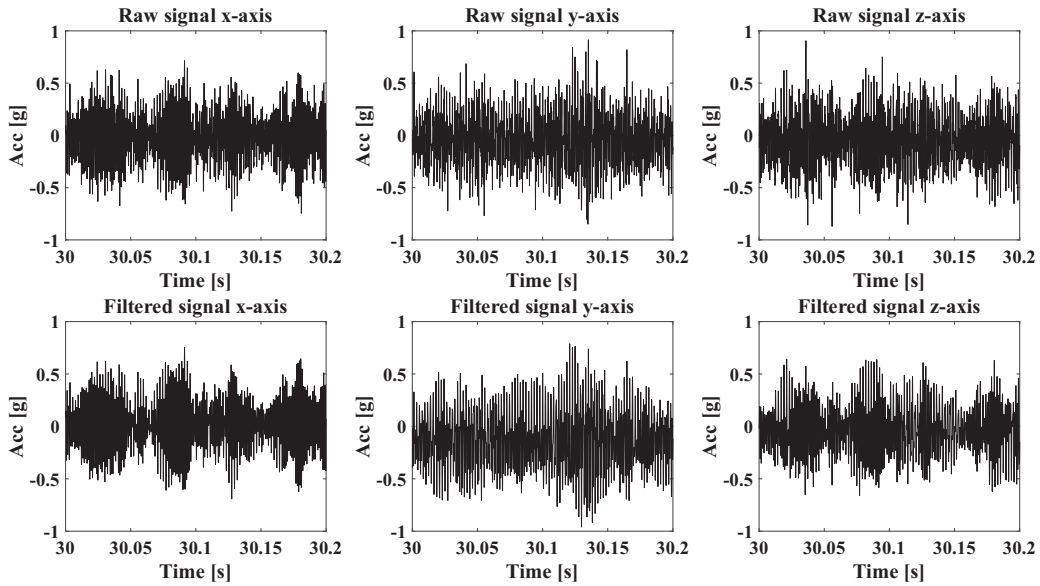

Fig. 7. Raw and filtered gearbox vibration for Signal 1.

- 36, 72, 108, 144, 180, 216, 252, and 288 for the FG;
- 90, 180, and 270 for the CG.

This approach ensures a balance between capturing relevant fault signatures and minimizing noise, thereby enhancing the reliability and reproducibility of the FD process.

In the present study, the effectiveness of VKF_MOT is demonstrated as showed in Fig. 8 for the normalized raw and filtered gearbox vibration order spectrum for signal 1 of Table I.

Figure 8 shows the amplitude reduction of the unselected orders, considered as noise, and how the selected orders are correctly extracted: the use of VKF_MOT allows highlighting the selected orders that are characteristic of the faulty gear and allows to highlight the differences between the healthy and the defective. In addition, the bandwidth also considers orders around the selected orders. This is due to the chosen first-order filter: this bandwidth could have been reduced by adopting a second-order filter, but the computational cost would have increased [46]. The first-order $\pm 3dB$ passband filter of each tracked order is established equal to 0.5% of the sampling frequency f_s. Switching to a second-order structural equation halves the passband but quadruples the state dimension and roughly octuplets the floating-point operations [47]. The work aim is to demonstrate that the proposed pipeline can enhance the SDP-CNN combination for detecting the incipient defects in gear under variable working conditions.

The raw and filtered signals were divided into segments of three faulty gear revolutions and transformed using SDP. This choice is useful to further highlight the defects that will have to differentiate the SDP diagrams, and it is made to obtain as many images as possible to train, validate, and test the developed CNNs. Figure 9 shows a comparison between the snowflakes of raw and filtered signals for one segment.

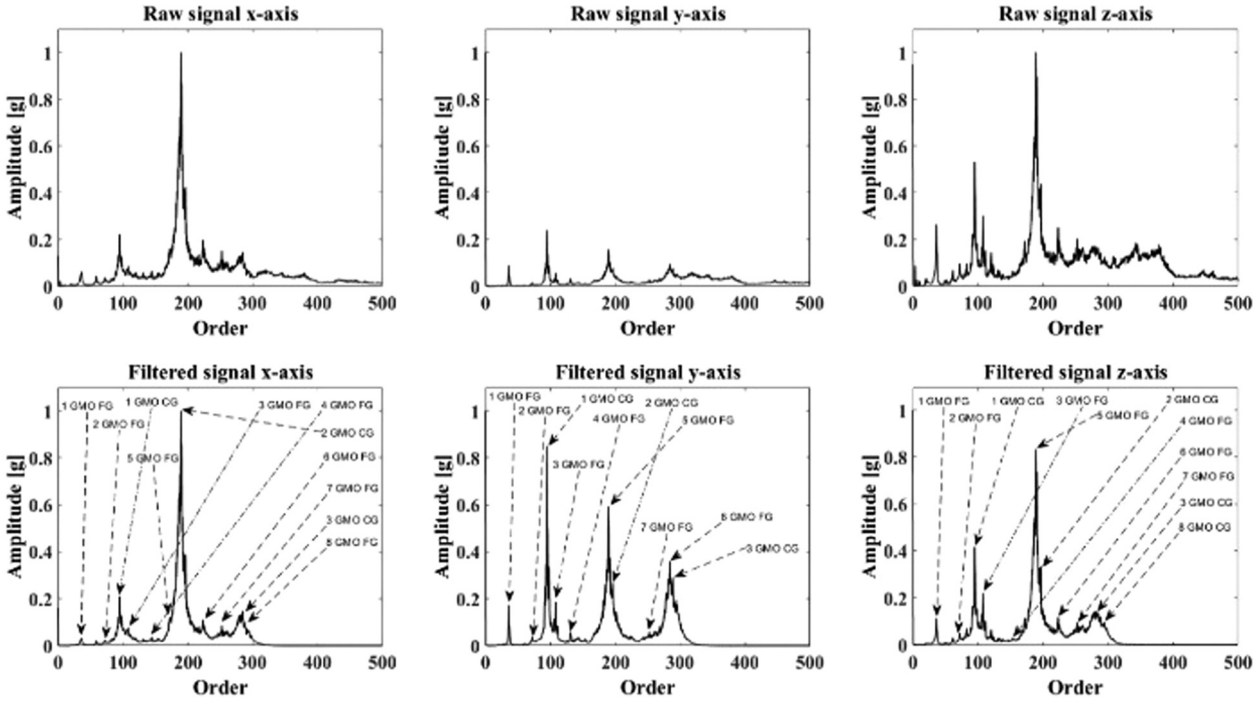

Fig. 8. Raw and filtered gearbox vibration order spectrum for signal 1.

The SDP diagrams in Fig. 9 were obtained by setting $\xi = 30$ and $l = 7$. These SDP parameters are empirically chosen to prevent the petals from overlapping [41]. The generic snowflake diagram in Fig. 9 was obtained by composing the SDP transformation of vibrational signals sampled along the three axes.

The simultaneous use of all three axes in the same snowflake allows for greater differentiation of SDP diagrams. In Fig. 9, the SDP diagrams of raw signals appear visually complex and overlapped with patterns showing some symmetry that tends to mask morphological differences between fault classes. Indeed, the Pitting and Break conditions present very similar shape in the raw signals, making clear distinction difficult. Moreover, the presence of high-frequency noise and the dispersion of the data points compromise class separability. Instead, the diagrams obtained from the filtered signals show more distinct shapes and sharper contours across conditions. Filtering reduces the influence of noise while preserving the main informative components, thereby enhancing the dynamic features associated with each fault mode. For example, the Wear case exhibits a marked reduction in amplitude along the x-axis, whereas Break produces a very regular and distinct symmetry. These differences become easier to interpret both visually and computationally, facilitating the application of automatic classification techniques. Specifically, SDP diagrams from the filtered signals in Fig. 9 highlight:

- Healthy has a regular, balanced pattern with homogeneous amplitudes and well-distributed symmetry across the three axes.
- Wear reduced amplitude on the x-axis, resulting in a compressed shape compared to the healthy state. This characteristic is hard to detect in the raw diagram due to noise masking.

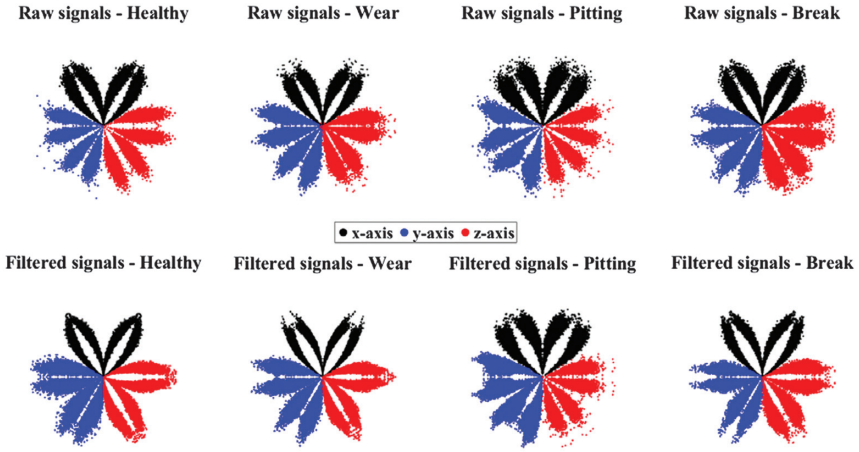

Fig. 9. Comparison between SDP transformation of raw and filtered signals.

- Pitting is clearly asymmetric across axes, with greater spread along the z-axis. This pattern is not visible in the raw signals by high-frequency components.
- Break shows a highly regular and strongly extended pattern, particularly along the x and y axes, with marked symmetries reflecting structural compromise. Unlike Pitting, this distinction is clear only after filtering.

The improvement in class separation achieved through filtering is attributable to removing spectrally non-informative components while preserving defects characteristic frequencies. This makes the SDP transform more effective as a diagnostic tool.

The obtained SDP diagrams were used as input for the developed CNNs: the dataset was divided into 50% for training, 20% for validation, and the remaining 30% for testing.

The first step to validate the proposed methodology was to develop two-class CNNs to discriminate between the health state and one of the defects shown in Table I. For each optimization process, a minimum set of 50 iterations was set to interrupt the Bayesian optimization process using the expected improvement criterion. Each CNN was trained for 1000 epochs with a validation frequency every 10 epochs. A PC with a processor 13th Gen Intel Core i9-13900 of 2.00 GHz, 32 GB of RAM, and a 12 GB NVIDIA GeForce RTX 3060 was used. Table II reports the optimized hyperparameter ranges.

In Fig. 10 are reported the trend of the errors during the Bayesian Optimization process for each CNN where it can be observed that the error achieved by CNNs for the VKF_MOT-SDP-CNN pipeline is always lower than the SDP-CNN one.

Furthermore, in Table III the computational time for each optimization process is reported, while the CNN testing accuracy is reported in Table IV.

Comparing the CNN accuracy between the SDP diagram obtained from the raw and the filtered signals of Table IV, it is possible to note that the accuracy always increases using the VKF_MOT for pre-processing the signals.

The receiver operating characteristic (ROC) [48] curve for each CNN was calculated to evaluate the false positive rate. The ROC curves were reported in Fig. 11, while the corresponding area under the curve (AUC) was reported in Table V.

Table II. Hyperparameter range

Hyperparameter	Range
Convolutional Layers	1÷4
Stride of Convolutional Layers	2÷5
Filters Size of Convolutional Layers	1÷5
Filters Numbers of Convolutional Layers	2÷50
Stride of Pooling	2÷5
Pooling Size	1÷5
Fully Connected Layers Number	1÷5
Neurons Numbers of Fully Connected Layers	1÷1000
Initialization Learning Rate	10^{-6}÷10^{-1}
Momentum	0.01÷0.99
Mini Batch Size	2÷256
L2 Regularization	10^{-6}÷10^{-1}

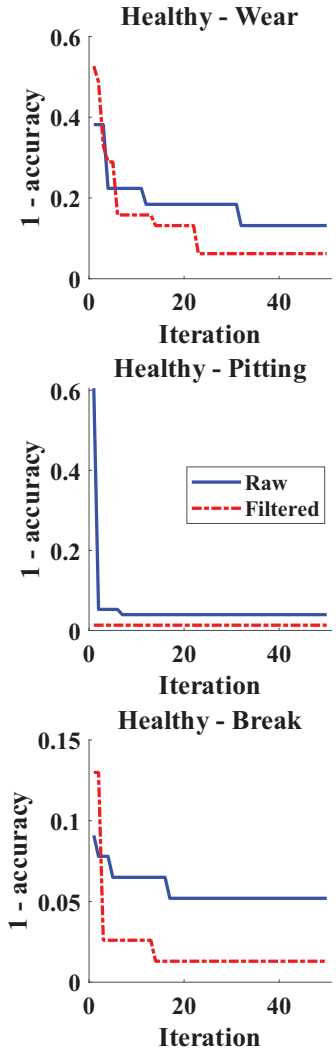

Fig. 10. CNN Bayesian Optimization process.

Looking at the ROC curves in Fig. 11, it is possible to see that the filtered cases have a greater tendency toward the point (0,1) than the raw cases: this means that the false positive rate is lower in the filtered case than in the raw case. This result was confirmed by the AUC reported in Table V.

Finally, a multi-class CNN network was developed to classify whether the input SDP diagram belongs to the gear healthy state, or it is related to an incipient defect. The comparison between the classical and the proposed technique was carried out: the CNN Bayesian optimization process errors are reported in Fig. 12, in Table VI is reported the computational time, the test accuracy is shown in Table VII, Fig. 13 shows the One vs Rest ROC curve (Wear, Break, and Pitting defects as positive class), and Table VIII shows the AUC.

Table III. Computational time of CNN optimization process

CNN classes	Raw signals	Filtered signals
Healthy – Break	00:42:08	01:05:33
Healthy – Pitting	00:52:27	00:50:55
Healthy – Wear	01:06:04	00:39:23

Table IV. CNN testing accuracy

CNN classes	% accuracy of raw signals	% accuracy of filtered signals	% difference
Healthy – Break	89.65	95.69	+6.04
Healthy – Pitting	96.55	97.41	+0.86
Healthy – Wear	85.34	91.52	+6.18

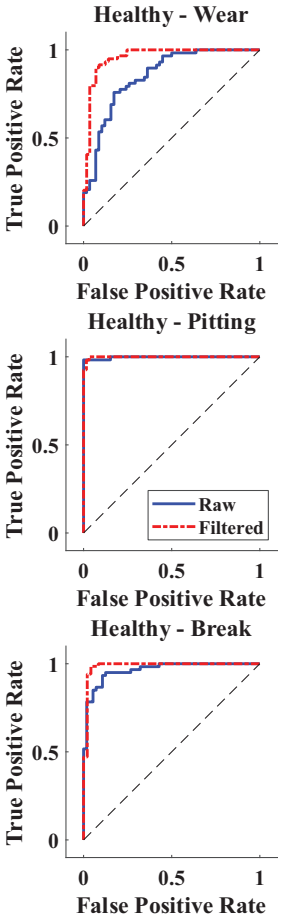

Fig. 11. ROC curves for CNNs.

The validity of the new technique is confirmed by Table VII, which shows an increase of 11% in the pre-processing of the signals using the VKF_MOT compared to the raw signals. The improvement is still evident when comparing the two One vs Rest ROC curve (Fig. 13) and the AUC values (Table VIII).

Finally, a comparison with other ML techniques applied on the same dataset is proposed. The comparison is reported in Table IX where the last column shows the difference between the accuracy of the proposed technique and that obtained in literature.

Table V. AUC of CNN testing results

CNN classes	AUC of raw signals	AUC of filtered signals	Percentage AUC difference
Healthy – Break	0.964	0.987	+ 2.3
Healthy – Pitting	0.997	0.998	+ 1.0
Healthy – Wear	0.853	0.958	+ 10.5

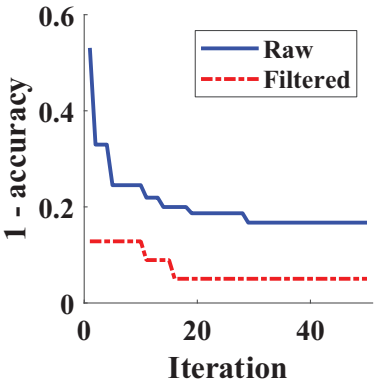

Fig. 12. CNN Bayesian Optimization process.

Table VI. Computational time of CNN optimization process

CNN classes	Raw signals	Filtered signals
Healthy – Break – Pitting – Wear	1:20:13	1:37:08

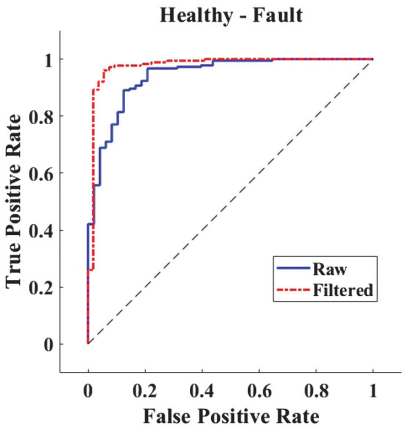

Fig. 13. One vs Rest ROC curve.

The proposed VKF_MOT-SDP-CNN achieves a lower accuracy compared to [49,50], but it offers a more intuitive visual interface for less experienced operators by allowing

Table VII. CNN testing accuracy

CNN classes	% accuracy of raw signals	% accuracy of filtered signals	% difference
Healthy – Break – Pitting – Wear	80.95	92.64	+11.69

Table VIII. AUC of CNN testing results

CNN classes	AUC of raw signals	AUC of filtered signals	Percentage AUC difference
Healthy vs Break – Pitting – Wear	0.942	0.977	+0.035

Table IX. Comparison with other techniques

References	Technique	Advantages	Disadvantages	Accuracy [%]	Comparison [%]
Sun *et al.* [49]	STNG and GCAIPN	• Robustness with small data • Local and global feature extraction	• High computational cost • Hypersensitivity to segmentation parameters	96.25	–3.61
Zhang *et al.* [50]	MVML-LCLLC	• Application even in case of missing or incomplete labels • Multi-labels	• High computational cost • Offline applications only	97.30	–4.66
Shao *et al.* [51]	PLL-WCAN	• High robustness • High generalization	• High computational cost • Complex hyperparameter tuning	92.20	+0.44

the direct observation of distinct patterns; indeed, [49] requires feature extraction across multiple domains. Moreover, its hyperparameter optimization is fully automated, unlike the approach in [50]. The proposed method reaches an accuracy comparable to what reported by Shao *et al*. [51].

V. CONCLUSIONS

The SDP transforms vibration signals into symmetrical visual patterns to facilitate the FD process, improves clarity, and makes it easier to recognize distinctive features, thereby improving the fault diagnosis process, compared to raw signal analysis. The work aimed to enhance the SDP-CNN combination for detecting incipient defects in gear under variable working conditions. For this purpose, a new pipeline was developed: first, a filtering of the vibration signals with VKF_MOT, then a transformation of the signals with the SDP technique, and finally the development of a CNN for gear FD. The method was validated on an experimental dataset including trapezoidal load-time curves and ramp speed-time curves.

Two-class CNNs were developed between the healthy state and an incipient defect, then a final CNN was developed to distinguish between the healthy and defective types. The new pipeline was compared with the classical SDP-CNN approach: the experimental results demonstrate the higher classification accuracy of the new approach compared to the classical one. These findings were also confirmed by ROC curve analysis and AUC calculation. Finally, the proposed technique was compared with other literature research demonstrating a slight decrease in accuracy, but with a more intuitive interpretation of the diagrams and with simpler hyperparameter optimization.

The proposed technique experimentally validated the VKF_MOT-SDP-CNN pipeline for gear FD under variable working conditions for incipient defects. The new method shows high accuracy, but it is computationally expensive due to VKF_MOT. In order to implement a VKF_MOT filter, it is necessary to acquire both the rotational speed of the system and the vibrational signal to be filtered. In practical applications, an encoder or tachometer sensor is usually available to derive the system rotational speed, so this dependency is not a limitation of VKF_MOT applicability in practical scenarios.

Future research will include the ability to assess the presence of combined defects and testing on different gearbox components such as bearings. It will also be possible to compare with other signal pre-processing techniques and combine the SDP diagram using signals of a different nature, such as vibration and rotational speed. To further improve the capabilities of feature representation in fault diagnosis, the integration of advanced embedding techniques could be explored. These methodologies could provide valuable insights into developing more robust and generalized fault diagnosis systems. Future work should also consider implementing the new pipeline in online monitoring systems, leveraging hardware acceleration such as FPGA-based platform. This would enable real-time monitoring of an industrial gearbox and allow for studying the trade-off between performance and hardware resource usage.

ACKNOWLEDGEMENT

The authors would like to thank Davide Merola for his contribution during the thesis work.

CONFLICT OF INTEREST STATEMENT

The authors declare no conflicts of interest.

FUNDING

This research received no external funding.

DATA AVAILABILITY STATEMENT

The raw data used in this research were a public dataset described in reference [37]. The processed data are not publicly available but may be obtained from the corresponding author upon reasonable request.

REFERENCES

[1] O. D. Mohammed and M. Rantatalo, "Gear fault models and dynamics-based modelling for gear fault detection–a review," *Eng. Fail. Anal.*, vol. 117, p. 104798, 2020.

[2] D. Sahu, R. K. Dewangan, and S. P. S. Matharu, "An investigation of fault detection techniques in rolling element bearing," *J. Vib. Eng. Technol.*, vol. 12, no. 4, pp. 5585–5608, 2024.

[3] S. Zhi, H. Shen, and T. Wang, "Gearbox localized fault detection based on meshing frequency modulation analysis," *Appl. Acoust.*, vol. 219, p. 109943, 2024.

[4] B. El Yousfi, A. Soualhi, K. Medjaher, and F. Guillet, "Electromechanical modeling of a motor–gearbox system for local gear tooth faults detection," *Mech. Syst. Signal Process.*, vol. 166, p. 108435, 2022.

[5] B. Hou, Y. Wang, B. Tang, Y. Qin, Y. Chen, and Y. Chen, "A tacholess order tracking method for wind turbine planetary gearbox fault detection," *Measurement*, vol. 138, pp. 266–277, 2019.

[6] J. Park, M. Hamadache, J. M. Ha, Y. Kim, K. Na, and B. D. Youn, "A positive energy residual (PER) based planetary gear fault detection method under variable speed conditions," *Mech. Syst. Signal Process.*, vol. 117, pp. 347–360, 2019.

[7] L. Liu, L. Chen, Z. Wang, and D. Liu, "Early fault detection of planetary gearbox based on acoustic emission and improved variational mode decomposition," *IEEE Sens. J.*, vol. 21, no. 2, pp. 1735–1745, 2020.

[8] C. Cheng, X. Wang, S. Xu, K. Feng, and H. Chen, "Dynamic weighted slow feature analysis-based fault detection for running gear systems of high-speed trains," *Int. J. Control Autom. Syst.*, vol. 22, no. 6, pp. 1924–1934, 2024.

[9] P. Zhou, Z. Peng, S. Chen, Z. Tian, and M. J. Zuo, "Sinusoidal FM patterns of fault-related vibration signals for planetary gearbox fault detection under non-stationary conditions," *Mech. Syst. Signal Process.*, vol. 155, p. 107623, 2021.

[10] J. Yuan, Z. Yao, Q. Zhao, Y. Xu, C. Li, and H. Jiang, "Dual-core denoised synchrosqueezing wavelet transform for gear fault detection," *IEEE Trans. Instrum. Meas.*, vol. 70, pp. 1–11, 2021.

[11] X. Tao et al., "Bearings fault detection using wavelet transform and generalized Gaussian density modeling," *Measurement*, vol. 155, p. 107557, 2020.

[12] Q. Li, B. Chen, Q. Chen, X. Li, Z. Qin, and F. Chu, "HSE: a plug-and-play module for unified fault diagnosis foundation models," *Inf. Fusion*, vol. 123, p. 103277, 2025.

[13] Q. Li, H. Li, W. Hu, S. Sun, Z. Qin, and F. Chu, "Transparent operator network: a fully interpretable network incorporating learnable wavelet operator for intelligent fault diagnosis," *IEEE Trans. Ind. Inform.*, vol. 20, no. 6, pp. 8628–8638, 2024.

[14] D. Neupane and J. Seok, "Bearing fault detection and diagnosis using Case Western Reserve University dataset with deep learning approaches: a review," *IEEE Access*, vol. 8, pp. 93155–93178, 2020.

[15] W. Lu, Y. Li, Y. Cheng, D. Meng, B. Liang, and P. Zhou, "Early fault detection approach with deep architectures," *IEEE Trans. Instrum. Meas.*, vol. 67, no. 7, pp. 1679–1689, 2018.

[16] H. Wang, R. Yang, and J. Xiang, "Numerical simulation of gears for fault detection using artificial intelligence models," *Measurement*, vol. 203, p. 111898, 2022.

[17] Y. Gao, X. Liu, and J. Xiang, "Fault detection in gears using fault samples enlarged by a combination of numerical simulation and a generative adversarial network," *IEEE/ASME Trans. Mechatron.*, vol. 27, no. 5, pp. 3798–3805, 2022.

[18] K. N. Ravikumar et al., "Gearbox fault diagnosis based on multi-scale deep residual learning and stacked LSTM model," *Measurement*, vol. 186, p. 110099, 2021.

[19] V. Niola et al., "Torque/speed equilibrium point monitoring of an aircraft hybrid electric propulsion system through accelerometric signal processing," *Appl. Sci.*, vol. 15, no. 4, p. 2135, 2025.

[20] C. A. Pickover, "On the use of symmetrized dot patterns for the visual characterization of speech waveforms and other sampled data," *J. Acoust. Soc. Am.*, vol. 80, no. 3, pp. 955–960, 1986.

[21] W. Xing-He, W. Hong-Jun, C. Ying-Jie, and L. Ze-Rui, "Classification and recognition method of bearing fault based on SDP-CNN," In *Proc. IncoME-VI and TEPEN 2021: Performance Engineering and Maintenance Engineering*. Cham, Switzerland: Springer Int. Publ., 2022, pp. 417–426.

[22] Z. Ren and J. Guo, "On fault diagnosis using image-based deep learning networks based on vibration signals," *Multimedia Tools Appl.*, vol. 83, no. 15, pp. 44555–44580, 2024.

[23] Y. Fu, X. Chen, Y. Liu, C. Son, and Y. Yang, "Gearbox fault diagnosis based on multi-sensor and multi-channel decision-level fusion based on SDP," *Appl. Sci.*, vol. 12, no. 15, p. 7535, 2022.

[24] W. Cui, G. Meng, T. Gou, A. Wang, R. Xiao, and X. Zhang, "Intelligent rolling bearing fault diagnosis method using symmetrized dot pattern images and CBAM-DRN," *Sensors*, vol. 22, no. 24, p. 9954, 2022.

[25] B. Pang, J. Liang, H. Liu, J. Dong, Z. Xu, and X. Zhao, "Intelligent bearing fault diagnosis based on multi-variate symmetrized dot pattern and LEG transformer," *Mach.*, vol. 10, no. 7, p. 550, 2022.

[26] T. E. Wu, S. H. Huang, and C. H. Lai, "Helical gear defect detection system based on symmetrized dot pattern and convolutional neural network," *IEEE Access*, vol. 12, pp. 171328–171333, 2024.

[27] J. D. Wu, W. J. Luo, and K. C. Yao, "Acoustic signal classification using symmetrized dot pattern and convolutional neural network," *Mach.*, vol. 10, no. 2, p. 90, 2022.

[28] X. Zhu, D. Hou, P. Zhou, Z. Han, Y. Yu-An, W. Zhou, and Q. Yin, "Rotor fault diagnosis using a convolutional neural network with symmetrized dot pattern images," *Measurement*, vol. 138, pp. 526–535, 2019.

[29] J. Song, H. Han, X. Wu, J. Lu, X. Wang, and S. Lu, "Multisource deep feature fusion of optimized symmetrized dot patterns for SRM fault diagnosis," *IEEE Trans. Instrum. Meas.*, vol. 73, p. 3520313, 2024.

[30] C. Zhang, W. Wang, and H. Li, "Tool wear prediction method based on symmetrized dot pattern and multi-covariance Gaussian process regression," *Measurement*, vol. 189, p. 110466, 2022.

[31] X. Xu, H. Liu, H. Zhu, and S. Wang, "Fan fault diagnosis based on symmetrized dot pattern analysis and image matching," *J. Sound Vib.*, vol. 374, pp. 297–311, 2016.

[32] X. Xu, M. Qi, and H. Liu, "Real-time stall detection of centrifugal fan based on symmetrized dot pattern analysis and image matching," *Measurement*, vol. 146, pp. 437–446, 2019.

[33] Y. Sun, S. Li, Y. Wang, and X. Wang, "Fault diagnosis of rolling bearing based on empirical mode decomposition and improved Manhattan distance in symmetrized dot pattern

image," *Mech. Syst. Signal Process.*, vol. 159, p. 107817, 2021.

[34] G. Tang, H. Hu, J. Kong, and H. Liu, "A novel fault feature selection and diagnosis method for rotating machinery with symmetrized dot pattern representation," *IEEE Sens. J.*, vol. 23, no. 2, pp. 1447–1461, 2023.

[35] F. Yang, X. Tian, L. Ma, and X. Shi, "An optimized variational mode decomposition and symmetrized dot pattern image characteristic information fusion-based enhanced CNN ball screw vibration intelligent fault diagnosis approach," *Measurement*, vol. 229, p. 114382, 2024.

[36] J. Liu, Q. Zhang, F. Xie, X. Wang, and S. Wu, "Incipient fault detection of planetary gearbox under steady and varying condition," *Expert Syst. Appl.*, vol. 233, p. 121003, 2023.

[37] S. Chen, Z. Liu, X. He, D. Zou, and D. Zhou, "Multi-mode fault diagnosis datasets of gearbox under variable working conditions," *Data Brief*, vol. 54, p. 110453, 2024.

[38] M. C. Pan and Y. F. Lin, "Further exploration of Vold–Kalman-filtering order tracking with shaft-speed information —I: theoretical part, numerical implementation and parameter investigations," *Mech. Syst. Signal Process.*, vol. 20, no. 5, pp. 1134–1154, 2006.

[39] M. C. Pan and Y. F. Lin, "Further exploration of Vold–Kalman-filtering order tracking with shaft-speed information —II: engineering applications," *Mech. Syst. Signal Process.*, vol. 20, no. 6, pp. 1410–1428, 2006.

[40] M. C. Pan and C. X. Wu, "Adaptive Vold–Kalman filtering order tracking," *Mech. Syst. Signal Process.*, vol. 21, no. 8, pp. 2957–2969, 2007.

[41] J. González, J. M. F. Oro, L. Delgado, D. Mendez, K. M. Argüelles, S. Velarde-Suárez, and D. Rodriguez, "Symmetrized dot pattern analysis for the unsteady vibration state in a Sirocco fan unit," *Appl. Acoust.*, vol. 152, pp. 1–12, 2019.

[42] S. Khan, H. Rahmani, S. A. A. Shah, M. Bennamoun, G. Medioni, and S. Dickinson, *A Guide to Convolutional Neural Networks for Computer Vision*. Cham, Switzerland: Springer, 2018.

[43] J. Wu, X. Y. Chen, H. Zhang, L. D. Xiong, H. Lei, and S. H. Deng, "Hyperparameter optimization for machine learning models based on Bayesian optimization," *J. Electron. Sci. Technol.*, vol. 17, no. 1, pp. 26–40, 2019.

[44] L. Hong, J. S. Dhupia, and S. Sheng, "An explanation of frequency features enabling detection of faults in equally spaced planetary gearbox," *Mech. Mach. Theory*, vol. 73, pp. 169–183, 2014.

[45] I. Lupea, M. Lupea, and A. Coroian, "Helical gearbox defect detection with machine learning using regular mesh components and sidebands," *Sensors*, vol. 24, no. 11, p. 3337, 2024.

[46] H. Vold, H. Herlufsen, M. Mains, and D. Corwin-Renner, "Multi axle order tracking with the Vold-Kalman tracking filter," *Sound Vib.*, vol. 31, no. 5, pp. 30–35, 1997.

[47] J. Tuma, "Setting the passband width in the Vold-Kalman order tracking filter," in *Proc. 12th Int. Congr. Sound Vib. (ICSV12)*, July 2005, pp. 1–8.

[48] W. J. Krzanowski and D. J. Hand, *ROC Curves for Continuous Data*. Boca Raton, FL, USA: Chapman and Hall/CRC, 2009.

[49] S. Sun, X. Xia, and H. Zhou, "A graph representation learning-based method for fault diagnosis of rotating machinery under time-varying speed conditions," *Nonlinear Dyn.*, vol. 113, pp. 17449–17475, 2025.

[50] W. Zhang, J. He, C. Ma, W. Gao, and G. Li, "Compound fault diagnosis method of rotating machinery using multi-view multi-label feature selection based on label compression and local label correlation," *Adv. Eng. Inform.*, vol. 65, p. 103310, 2025.

[51] Z. Shao, H. Jiang, X. Zhang, J. Zhou, and W. Huang, "PLL-WCAN: pseudo-label progressive learning guided wavelet class-aware adaptive network for gearbox cross-domain fault diagnosis," *Mech. Syst. Signal Process.*, vol. 230, p. 112624, 2025.